Performance of Flux Density Based Control Approaches for Active Magnetic Bearings – an Overview

Robin Liebfried[a] and Wilfried Hofmann[a]
[a] Technische Universiät Dresden, Elektrotechnisches Institut, Helmholtzstraße 9, 01062 Dresden, Germany,
robin.liebfried@tu-dresden.de

***Abstract*—Direct flux density control of active magnetic bearings is a promising approach to increase controller accuracy or reduce the system's price. New, ultra-thin Bismuth Hall Sensors provide the possibility to measure the air gap flux density directly. The paper presents the modelling of different bearing types and compares different control approaches with flux density measurement.**

***Index Terms*—active magnetic bearings, flux density measurement, Hall sensor, direct field control, state space control, cascade control, pole placement, optimal control, eddy current, comparison, modelling**

I. Introduction

Active magnetic bearings (AMB) are more and more commonly used in high-speed applications (e.g. flywheel accumulators) because of the low friction losses. Additionally, they can be used for active damping of spindle drives. Since an AMB is a non-linear, inherently unstable system, the design of the control strategy is very important for the dynamic stability and accuracy of the drive. The most straightforward control approach is a displacement control with an inner current control loop. This is the state of the art and has proven to offer decent robustness and precision.

In order to improve the precision of positioning and the dynamic stiffness of AMB, flux based control algorithms were suggested in [1]. A direct flux control requires real-time data of the air gap flux density which can be acquired by observers [2] or measurements. The latter is a possibility for low-cost AMB operating without expensive position gauges [3].

To measure the air gap flux density, Hall sensors need to be placed within the air gap. With nominal air gap distances of 500 µm or less, ultra-thin sensors are required. Recent research shows promising results in fabricating 100 µm thin Bismuth Hall sensors that enable air gap integrated flux density measurement [4], [5].

After a proof-of-concept of these new Hall sensors were presented in [6], this paper focuses on a more detailed analysis and comparison of direct flux control strategies with flux density measurement. The test rig consists of a radial hybrid bearing (HB) as the first radial bearing and a combined radial/thrust hybrid bearing (CB) to complete the five-axis bearing. A motor between the HB and the CB allows rotation up to 3000 rpm. The control algorithms are tested in a full five-axis Matlab Simulink simulation including the influence of the voltage source converter (VSC). Fig. 1 shows the set-up of the test rig.

This paper presents calculations and boundary conditions for the flux-based model (section II). Then, cascaded current control and cascaded flux density control (section III) will be introduced. A state space control approach with different pole placement options is presented in section IV will be introduced. The paper concludes with a comparison and further optimisation approaches (section V).

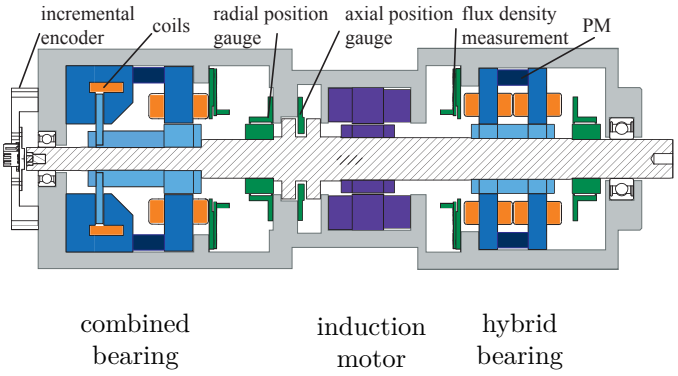

Fig. 1. Drawing of the test rig with the combined radial/thrust bearing left and the hybrid bearing right

II. AMB Model

The model of the AMB consist of an inverter, the flux density plant and the mechanical model. The inverter is represented by a time delay T_{vsc}. The mechanical model uses the reduced mass[1] m_{r} and a double integration to find the position x from the force F

$$x(s) = \frac{1}{m_{\mathrm{r}} s^2} F(s)\,. \tag{1}$$

A. Magnetic force

Since the magnetic force model is non linear, it is linearised around the desired operation point (shaft in the centre of the AMB). Fig. 2 shows the HB setup for the x-axis. Considering the attracting magnetic force for one pole with air gap area A_δ as

$$F_{\mathrm{p}} = \frac{B^2 A_\delta}{2\mu_0} = \frac{\Phi^2}{2\mu_0 A_\delta}\,. \tag{2}$$

The total force applied to the shaft by the HB in one direction (here x-axis) F_{x} can be described as

$$F_{\mathrm{x\,HB}} = (F_{\mathrm{x1l}} + F_{\mathrm{x1r}}) - (F_{\mathrm{x2l}} + F_{\mathrm{x2r}}) \tag{3}$$

[1]The reduced mass describes the mass which actually needs to be accelerated by the bearing. It considers the shaft's centre of gravity, weight force and mass moment of inertia.

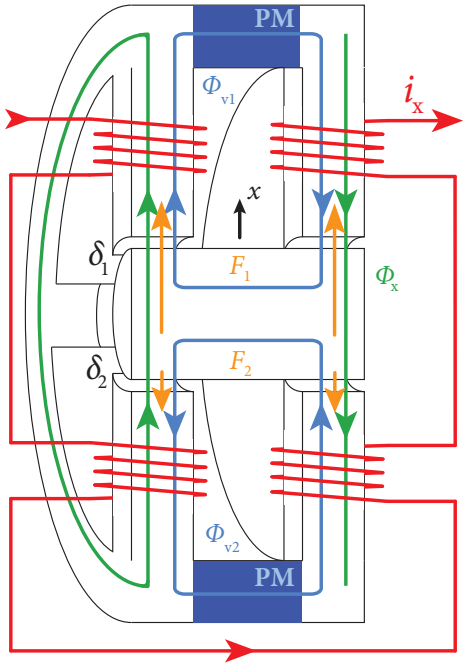

Fig. 2. Setup, flux and current definitions for the x-axis of the hybrid bearing

with indices l and r for left and right, respectively. The left and the right side of the HB are identical, so that (3) with (2) yields

$$F_{\mathrm{x\,HB}} = \frac{2(\Phi_{\mathrm{vx1}} + \Phi_{\mathrm{xx1}})^2 - 2(\Phi_{\mathrm{vx2}} - \Phi_{\mathrm{xx2}})^2}{2\mu_0 A_\delta} \,. \tag{4}$$

For the calculation of the radial forces, the CB can be considered half an HB. This leads to

$$F_{\mathrm{x\,CB}} = \frac{(\Phi_{\mathrm{vx1}} + \Phi_{\mathrm{xx1}})^2 - (\Phi_{\mathrm{vx2}} - \Phi_{\mathrm{xx2}})^2}{2\mu_0 A_\delta} \,. \tag{5}$$

The thrust bearing has one disc where the CM's total PM flux splits to the bias flux in z-direction Φ_{vz1} and the bias flux in negative z-direction Φ_{vz2}. The axial control flux Φ_{xz} is constant over the disc's active area so that the force is

$$F_{\mathrm{z}} = \frac{(\Phi_{\mathrm{vz1}} + \Phi_{\mathrm{xz}})^2 - (-\Phi_{\mathrm{vz2}} + \Phi_{\mathrm{xz}})^2}{2\mu_0 A_\delta} \,. \tag{6}$$

The index HB will not be explicitly indicated in the following sections. All calculations refer to the HB unless otherwise stated.

B. Magnetic equivalent circuit – bias flux

In order to calculate Φ_{v} and Φ_{x}, the reluctances of the system are required. Neglecting the iron reluctance for the bias flux because of the permanent magnets (PM) with $\mu_{\mathrm{rPM}} \approx 1$ and $\mu_{\mathrm{rFE}} \gg 1$ leads to the magnetic equivalent circuit shown in Fig. 3. Now considering that the left and the right half of the HB are identical and the permanent magnets are symmetrically placed within the bearing, we can simplify the circuit in Fig. 3. For the middle PM part it yields

$$\Theta_{\mathrm{PMx1}} = \Theta_{\mathrm{PMx2}} = \Theta_{\mathrm{PMy1}} = \Theta_{\mathrm{PMy2}} = \Theta_{\mathrm{PM}} \tag{7}$$

$$R_{\mathrm{mPMx1}} = R_{\mathrm{mPMx2}} = R_{\mathrm{mPMy1}} = R_{\mathrm{mPMy2}} = R_{\mathrm{mPM}} \tag{8}$$

$$\Phi_{\mathrm{PMx1}} + \Phi_{\mathrm{PMx2}} + \Phi_{\mathrm{PMy1}} + \Phi_{\mathrm{PMy2}} = \Phi_{\mathrm{PM}} \tag{9}$$

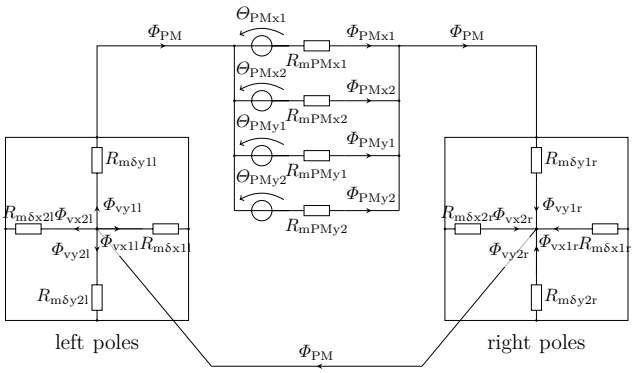

Fig. 3. Magnetic equivalent circuit of the HB for bias flux

and for the radial air gaps

$$R_{\mathrm{m\delta x}\nu\mathrm{l}} = R_{\mathrm{m\delta x}\nu\mathrm{r}} = R_{\mathrm{m\delta x}\nu} \tag{10}$$

$$R_{\mathrm{m\delta y}\nu\mathrm{l}} = R_{\mathrm{m\delta y}\nu\mathrm{r}} = R_{\mathrm{m\delta y}\nu} \tag{11}$$

$$\Phi_{\mathrm{vx}\nu\mathrm{l}} = \Phi_{\mathrm{vx}\nu\mathrm{r}} = \Phi_{\mathrm{vx}\nu} \tag{12}$$

$$\Phi_{\mathrm{vy}\nu\mathrm{l}} = \Phi_{\mathrm{vy}\nu\mathrm{r}} = \Phi_{\mathrm{vy}\nu} \tag{13}$$

with $\nu = \{1, 2\}$. The reluctances R_{m} can be calculated with the nominal, radial air gap distance δ_{r} and the pole air gap area A_δ. They depend on the shaft's position.

$$R_{\mathrm{m\delta x1}} = \frac{\delta_{\mathrm{r}} - x}{\mu_0 A_\delta} \,, \qquad R_{\mathrm{m\delta x2}} = \frac{\delta_{\mathrm{r}} + x}{\mu_0 A_\delta} \,, \tag{14}$$

$$R_{\mathrm{m\delta y1}} = \frac{\delta_{\mathrm{r}} - y}{\mu_0 A_\delta} \,, \qquad R_{\mathrm{m\delta y2}} = \frac{\delta_{\mathrm{r}} + y}{\mu_0 A_\delta} \,, \tag{15}$$

$$R_{\mathrm{mPM}} = \frac{l_{\mathrm{PM}}}{\mu_0 \mu_{\mathrm{rPM}} A_{\mathrm{PM}}} \,, \qquad R_{\mathrm{m\delta 0}} = \frac{\delta_{\mathrm{r}}}{\mu_0 A_\delta} \,. \tag{16}$$

The combined air gap reluctance $R_{\mathrm{m}\delta}(x, y)$ for the left and the right poles of the HB can be calculated by the rules of parallel connection. The x- and y-axis should be controlled independently, therefore $y = 0$ is assumed for analysing the x-axis (and vice versa). This leads to

$$\begin{aligned} R_{\mathrm{m}\delta}(x, y = 0) &= R_{\mathrm{m\delta x1}} \parallel R_{\mathrm{m\delta x2}} \parallel R_{\mathrm{m\delta y1}} \parallel R_{\mathrm{m\delta y2}} \\ &= R_{\mathrm{m\delta x1}} \parallel R_{\mathrm{m\delta x2}} \parallel \frac{1}{2} R_{\mathrm{m\delta 0}} \\ &= \frac{\delta_{\mathrm{r}}}{2\mu_0 A_\delta} \left(\frac{\delta_{\mathrm{r}}^2 - x^2}{2\delta_{\mathrm{r}}^2 - x^2} \right) \,. \end{aligned} \tag{17}$$

Eq. (14), (15) and (17) are used to calculate the bias flux of the poles

$$\frac{\Phi_{\mathrm{vx1}}}{\Phi_{\mathrm{PM}}} = \frac{R_{\mathrm{m}\delta}}{R_{\mathrm{m\delta x1}}} = \frac{\delta_{\mathrm{r}}(\delta_{\mathrm{r}} + x)}{2(2\delta_{\mathrm{r}}^2 - x^2)} \tag{18}$$

$$\frac{\Phi_{\mathrm{vx2}}}{\Phi_{\mathrm{PM}}} = \frac{R_{\mathrm{m}\delta}}{R_{\mathrm{m\delta x2}}} = \frac{\delta_{\mathrm{r}}(\delta_{\mathrm{r}} - x)}{2(2\delta_{\mathrm{r}}^2 - x^2)} \tag{19}$$

$$\frac{\Phi_{\mathrm{vy1}}}{\Phi_{\mathrm{PM}}} = \frac{\Phi_{\mathrm{vy2}}}{\Phi_{\mathrm{PM}}} = \frac{R_{\mathrm{m}\delta}}{R_{\mathrm{m\delta y}}} = \frac{(\delta_{\mathrm{r}}^2 - x^2)}{2\delta_{\mathrm{r}}^2 - x^2} \,. \tag{20}$$

Using (16), (17) and $\Theta_{\mathrm{PM}} = H_{\mathrm{c}} l_{\mathrm{PM}}(1 - k_{\mathrm{PM}})$ yields

$$\begin{aligned} \Phi_{\mathrm{PM}} &= \frac{\Theta_{\mathrm{PM}}}{R_{\mathrm{tot}}} = \frac{\Theta_{\mathrm{PM}}}{\frac{1}{4} R_{\mathrm{mPM}} + 2R_{\mathrm{m}\delta}} \\ &= \frac{4\,\mu_0 \mu_{\mathrm{rPM}}\, l_{\mathrm{PM}} A_{\mathrm{PM}} A_\delta\, H_{\mathrm{c}} k_{\mathrm{PM}} (2\delta_{\mathrm{r}}^2 - x^2)}{l_{\mathrm{PM}} A_\delta (2\delta_{\mathrm{r}}^2 - x^2) + \mu_{\mathrm{rPM}} A_{\mathrm{PM}} \delta_{\mathrm{r}} (\delta_{\mathrm{r}}^2 - x^2)} \end{aligned} \tag{21}$$

for $y = 0$ and where k_{PM} considers PM leakage and is found by experiments. Using the parameters from Table I, a

deviation of 0.11 % can be estimated when using $x = 0$ instead of $x = 50\,\mu\text{m}$ which is considered negligible and leads to (22).

$$\Phi_{\text{PM}}(x) \approx \Phi_{\text{PM}}(x=0) = \frac{8\,\mu_0\mu_{\text{rPM}}\,l_{\text{PM}}A_{\text{PM}}A_\delta\,H_{\text{c}}k_{\text{PM}}}{2l_{\text{PM}}A_\delta + \mu_{\text{rPM}}A_{\text{PM}}\delta_{\text{r}}} \tag{22}$$

With a non-displaced shaft the PM flux splits equally to all four poles and is called pole bias flux

$$\Phi_{\text{v}} = \frac{1}{4}\Phi_{\text{PM}}(x=0, y=0)\,. \tag{23}$$

For the bias flux density follows

$$B_{\text{v}} = \frac{\Phi_{\text{v}}}{A_\delta}\,. \tag{24}$$

Eq. (18), (19) and (22) can be used in (4). The calculations are valid for the y-axis analogously.

Similar calculations can be conducted for the CB. The "left poles" in Fig. 3 are replaced with the equivalent circuit for the thrust bearing – two parallel air gap reluctances

$$\begin{aligned} R_{\text{m}\delta\text{z}}(z) &= R_{\text{m}\delta\text{z1}} \parallel R_{\text{m}\delta\text{z2}} = \frac{\delta_{\text{a}}+z}{\mu_0\cdot A_{\text{s}}} \parallel \frac{\delta_{\text{a}}-z}{\mu_0\cdot A_{\text{s}}} \\ &= \frac{\delta_{\text{a}}^2 - z^2}{2\mu_0\delta_{\text{a}}A_{\text{s}}}\,. \end{aligned} \tag{25}$$

The total reluctance $R_{\text{tot CB}}$ of the CB is different to those of the HB. Therefore (22) changes to[2]

$$\Phi_{\text{PM CB}} = \frac{\Theta_{\text{PM CB}}}{\frac{1}{4}R_{\text{mPM}} + R_{\text{m}\delta\text{z}} + R_{\text{m}\delta}} \tag{26}$$

and

$$\Phi_{\text{v CB}} = \frac{1}{4}\Phi_{\text{PM CB}}(x=0, y=0, z=0) \tag{27}$$

can be defined for the bias flux in one radial bearing pole.

Eq. (18) to (20) are valid for the CB when considering the different parameters. The y-axis can be found analogously. Similar calculations for the thrust bearing yield

$$\frac{\Phi_{\text{vz1}}}{\Phi_{\text{PM CB}}} = \frac{R_{\text{m}\delta\text{z}}}{R_{\text{m}\delta\text{z1}}} = \frac{\delta_{\text{a}}+z}{2\delta_{\text{a}}} \tag{28a}$$

$$\frac{\Phi_{\text{vz2}}}{\Phi_{\text{PM CB}}} = \frac{R_{\text{m}\delta\text{z}}}{R_{\text{m}\delta\text{z2}}} = \frac{\delta_{\text{a}}-z}{2\delta_{\text{a}}}\,. \tag{28b}$$

C. Magnetic equivalent circuit – control flux

Due to $\mu_{\text{rPM}} \ll \mu_{\text{rFE}}$ the PM in Fig. 2 can be considered flux barriers for Φ_{x} and therefore the iron reluctance is not negligible for calculating Φ_{x}. This leads to the magnetic equivalent circuit in Fig. 4. R_{msz} is the reluctance of one stator tooth, R_{msr} represents the stator spine's reluctance. As in section II-B, $y = 0$ and $i_{\text{y}} = 0$ are assumed for analysing the x-axis. The stator iron reluctances can be conflated to R_{ms} using the symmetry of the circuit. The same can be done with the rotor iron reluctance R_{mrr} (not shown in Fig. 4), resulting in an iron equivalent reluctance for every axis

$$R_{\text{mFe}} = R_{\text{ms}} + R_{\text{mr}} = R_{\text{msz}} + \frac{R_{\text{msr}}}{8} + \frac{R_{\text{mrr}}}{8}\,. \tag{29}$$

This leads to significant simplifications shown in the lower circuit of Fig. 4 which can be solved analytically. Introducing

$$R_{\text{mx1}} = R_{\text{m}\delta\text{x1}} + R_{\text{mFe}}\,, \quad R_{\text{mx2}} = R_{\text{m}\delta\text{x2}} + R_{\text{mFe}}\,, \tag{30}$$

$$R_{\text{my}} = \frac{R_{\text{m}\delta 0} + R_{\text{mFe}}}{2}\,, \tag{31}$$

[2]Again, evaluating Φ_{PM} at $(x, y, z) = (0, 0, 0)$ leads to a negligible error compared with $\Phi_{\text{PM}}(x, y, z)$.

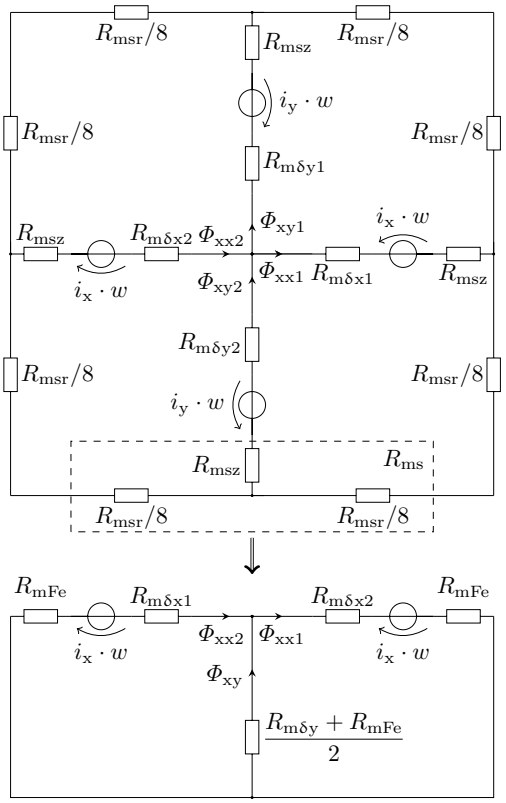

Fig. 4. Magnetic equivalent circuit of one side of the HB for control flux

the left and the right mash can be solved to

$$i_{\text{x}}\cdot w = \Phi_{\text{xx2}}\cdot R_{\text{mx2}} - \Phi_{\text{xy}}\cdot R_{\text{my}}\,, \tag{32a}$$

$$i_{\text{x}}\cdot w = \Phi_{\text{xx1}}\cdot R_{\text{mx1}} + \Phi_{\text{xy}}\cdot R_{\text{my}}\,, \tag{32b}$$

respectively. With

$$\Phi_{\text{xx1}} = \Phi_{\text{xx2}} + \Phi_{\text{xy}} \tag{33}$$

the control flux can be found:

$$\Phi_{\text{xx1}} = \frac{i_{\text{x}}\cdot w\cdot k_{\text{s}}\cdot(R_{\text{mx2}} + 2R_{\text{my}})}{R_{\text{mx1}}R_{\text{mx2}} + R_{\text{my}}(R_{\text{mx1}} + R_{\text{mx2}})} \tag{34a}$$

$$\Phi_{\text{xx2}} = \frac{i_{\text{x}}\cdot w\cdot k_{\text{s}}\cdot(R_{\text{mx1}} + 2R_{\text{my}})}{R_{\text{mx1}}R_{\text{mx2}} + R_{\text{my}}(R_{\text{mx1}} + R_{\text{mx2}})}\,. \tag{34b}$$

These calculations are valid for the y-axis and the CB analogously. The axial control flux can be calculated from the series connection of the two axial air gap reluctances $R_{\text{m}\delta\text{z1}} + R_{\text{m}\delta\text{z2}}$ and a constant reluctance R_{mFez} conflating all iron reluctances relevant for the thrust baring

$$\begin{aligned} \Phi_{\text{xz}} &= \frac{i_{\text{z}}\cdot w\cdot k_{\text{s}}}{R_{\text{m}\delta\text{z1}} + R_{\text{m}\delta\text{z2}} + R_{\text{mFez}}} \\ &= \frac{\mu_0\cdot A_{\text{s}}\cdot i_{\text{z}}\cdot w\cdot k_{\text{s}}}{2\delta_{\text{a}} + \mu_0 A_{\text{s}}R_{\text{mFez}}}\,. \end{aligned} \tag{35}$$

D. Linearisation

The resulting force for every axis of the AMB can now be calculated. The non-linear equations (4), (5) and (6) should be linearised in a form for current control

$$F(i, x) = k_{\text{i}}\cdot i + k_{\text{x}}\cdot x \tag{36}$$

or for flux density control

$$F(B_{\text{x}}, x) = k_{\text{B}}\cdot B_{\text{x}} + k_{\text{x}}\cdot x\,. \tag{37}$$

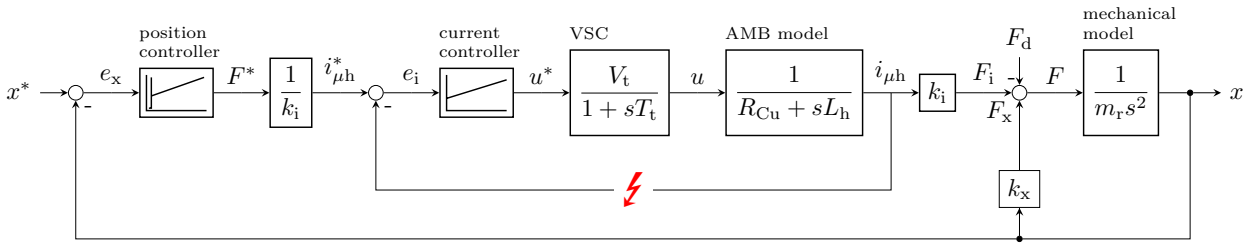

Fig. 5. Block diagram of the cascaded current control with linear AMB model $F = k_i i + k_x x$. Inner control loop was designed with amplitude optimum, outer with iterative optimisation. Parameters for HB are: $k_i = 37.9\,\text{N/A}$, $V_t = 1$, $T_t = 47\,\mu\text{s}$, $R_{Cu} = 0.26\,\Omega$, $L_h = 3.5\,\text{mH}$, $k_x = 213\,\text{kN/m}$, and $m_r = 1.56\,\text{kg}$.

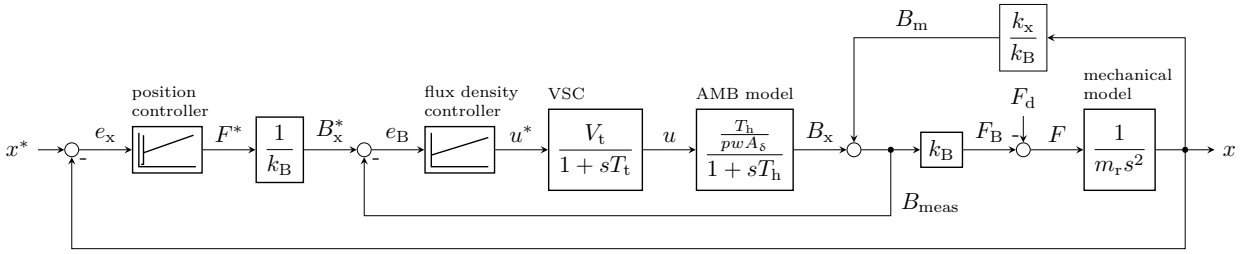

Fig. 6. Block diagram of the cascaded flux density control with linear AMB model $F = (B_x + B_m(x)) \cdot k_B$ with $B_m(x) = \frac{k_x}{k_B} x$. The outer loop controller is identical to Fig. 5. Additional parameters are $p = 2$ for HB, and $p = 1$ for CB.

A Taylor expansion is used to linearise the non-linear force equations around the bearing centre ($x = 0$, $y = 0$, $z = 0$, $\Phi_x = 0$) and find the factors k_i, k_x and k_B in (36) and (37):

$$k_{i\bullet} = \left.\frac{\partial F_\bullet(\Phi_{x\bullet}, a_\bullet)}{\partial i_{x\bullet}}\right|_{i_{x\bullet}=0, a_\bullet=0} \tag{38a}$$

$$k_{x\bullet} = \left.\frac{\partial F_\bullet(\Phi_{x\bullet}, a_\bullet)}{\partial a_{x\bullet}}\right|_{\Phi_{x\bullet}=0, a_\bullet=0} \tag{38b}$$

$$k_{B\bullet} = A_\bullet \cdot k_{\Phi\bullet} = \left.\frac{\partial F_\bullet(\Phi_{x\bullet}, a_\bullet)}{\partial \Phi_{x\bullet}}\right|_{\Phi_{x\bullet}=0, a_\bullet=0} \tag{38c}$$

where $\bullet$ indicates the corresponding bearing and axis and $a_\bullet$ the displacement in the direction of this axis[3]. The force equations for $F_\bullet$ can be taken from (4), (5) and (6). The needed expressions for substituting the bias flux $\Phi_{v\bullet}$ are given in (18), (19), (22), (26) and (28). The equations for the control flux $\Phi_{x\bullet}$ can be found in (34) and (35).

TABLE I. MODEL PARAMETERS

Parameter	Symbol	Value	Unit
Radial air gap	δ_r	0.5	mm
Axial air gap	δ_a	0.5	mm
Radial air gap area (HB)	$A_{\delta\,HB}$	2.24	cm^2
Radial air gap area (CB)	$A_{\delta\,CB}$	3.47	cm^2
Active disc area	A_s	38.2	cm^2
Rated force (HB)	$F_{n\,HB}$	108	N
Rated force radial (CB)	$F_{nr\,CB}$	143	N
Rated force axial (CB)	$F_{na\,CB}$	52.3	N
Mass of shaft	m	2.46	kg
Reduced mass (HB)	$m_{r\,HB}$	1.56	kg
Reduced mass (CB)	$m_{r\,CB}$	1.56	kg
Leakage coefficient	k_s	0.95	
PM leakage coefficient (HB)	$k_{PM\,HB}$	0.67	
PM leakage coefficient (CB)	$k_{PM\,CB}$	0.68	
PM Flux (HB)	$\Phi_{PM\,HB}$	349.8	µWb
PM Flux (CB)	$\Phi_{PM\,CB}$	708.9	µWb
Bias flux density (HB)	$B_{v\,HB}$	0.39	T
Bias flux density (CB)	$B_{v\,CB}$	0.51	T

[3]So $a_\bullet$ can be x, y, z.

The equation can be solved for the different bearing types to the terms given in Table II. All parameters additionally needed for the controller design are summarized in Table I.

TABLE II. LINEARISATION PARAMETERS FOR BOTH AMB TOPOLOGIES

Parameter	HB	CBr	CBa
k_i	$\frac{wk_s\Phi_{PM}}{\mu_0 A_\delta R_{mFe} + \delta_r}$	$\frac{0.5 \cdot wk_s\Phi_{PM}}{\mu_0 A_\delta R_{mFe} + \delta_r}$	$\frac{wk_s\Phi_{PM\,CB}}{\mu_0 A_s R_{mFez} + 2\delta_a}$
k_x	$\frac{\Phi^2_{PM}}{4\mu_0\delta_r A_\delta}$	$\frac{\Phi^2_{PM}}{8\mu_0\delta_r A_\delta}$	$\frac{\Phi^2_{PM\,CB}}{2\mu_0\delta_a A_s}$
k_B	$B_v\frac{4A_\delta}{\mu_0}$	$B_{v\,CB}\frac{2A_\delta}{\mu_0}$	$\frac{\delta_a\Phi_{PM\,CB}}{\mu_0(4\delta_0 + \mu_0 A_s R_{mFez})}$
k_i in N/A	38.30	61.60	57.56
k_x in N/mm	217.2	288.3	104.7
k_B in N/T	275.5	278.9	232.3

III. CASCADED CONTROL

All control algorithms are written in C and are called as s-functions in the MATLAB Simulink model for the AMB. The response to a 10 µm command value step and a 5 N disturbance force step are compared for the different approaches.

A. Current control

A cascaded current control (I-control) is designed as a state-of-the-art reference for the comparison. Fig. 5 shows the block diagram of the current control. The lightning indicates that this feedback is just correct without the consideration of eddy currents nor leakage because the measured current in total is assumed to be force creating [7]. Position measurement is mandatory for this control approach. The inner PI current controller is designed by the method of optimum amplitude for an optimal command response. A PID controller is needed for the outer position control loop due to the positive Feedback. For the design of the PID controller the AMB is described as a spring-damper system

$$F_{sd} = -k \cdot x - d \cdot \dot{x} \tag{39}$$

with stiffness k and damping d. Eq. (39) and (36) lead to an equation for the control current

$$i_\mathrm{x} = -\frac{(k+k_\mathrm{x})x + d\dot{x}}{k_\mathrm{i}} \,. \tag{40}$$

This system needs a PD controller for stabilisation which is technically not realisable. Therefore a PIDT2 controller

$$G_\mathrm{x} = K_\mathrm{px}\left(1 + \frac{1}{sT_\mathrm{ix}} + \frac{sT_\mathrm{d}}{s^2T_\mathrm{f}^2 + s2D_\mathrm{f}T_\mathrm{f} + 1}\right) \tag{41}$$

with

$$K_\mathrm{px} = \frac{k+k_\mathrm{x}}{k_\mathrm{i}} \qquad \text{and} \qquad T_\mathrm{d} = \frac{d}{k+k_\mathrm{x}} \tag{42}$$

is designed. k_x and k_i are given in Table II, k and d can be chosen regarding to the desired behaviour of the bearing. The stiffness is set $k = k_\mathrm{x}$ and Lehr's damping ratio $\xi = 0.3$ is used for finding the rate time [8], [9]

$$d = 2 \cdot m_\mathrm{r} \cdot \xi \cdot \omega_0 \quad \text{with} \quad \omega_0 = \sqrt{\frac{k}{m_\mathrm{r}}} \tag{43}$$

$$\Rightarrow T_\mathrm{d} = \frac{2 \cdot \xi \cdot \sqrt{k \cdot m_\mathrm{r}}}{k + k_\mathrm{x}} \,. \tag{44}$$

A small reset time T_i leads to quick a cancellation of control errors but T_i should be larger than the reciprocal of the natural frequency ω_0 (choice: $T_\mathrm{i} = 0.159\,\mathrm{s}$). The filter parameters are chosen so that measurement noise is filtered. This leads to $T_\mathrm{f} = 0.177\,\mathrm{ms}$ and $D_\mathrm{f} = 0.7$.

B. Flux density control

The flux density based control strategy (B-control) overcomes the drawbacks of the current control since the air gap flux density is directly force-creating and inherently considers eddy currents and leakage. The block diagram from Fig. 5 can be transformed into a cascaded flux density control (Fig. 6). The command response can be improved due to consideration of the displacement-dependent force as a disturbance in the faster, inner control loop. For the first attempt, the controllers are designed analogously to section III-A. The results compared to the I-control are shown in Fig. 7. Experiments show, that the disturbance $B_\mathrm{m}(x)$ causes steady state control errors, due to the small I-part of the inner PI-controller when designing the inner control loop with amplitude optimum (AO). Therefore, the flux density controller is designed with symmetrical optimum (SO) and $a = 3$ [10]. The results are also shown in Fig. 7. The design with SO shows less overshot and oscillation for command and disturbance response, so that the SO will be used subsequently.

IV. State Space Control

Due to the positive feedback, the outer loop controllers described above need a differential element to stabilise the system. This D-part causes a big overshoot. Model-based control approaches can overcome this problem and reduce the overshoot.

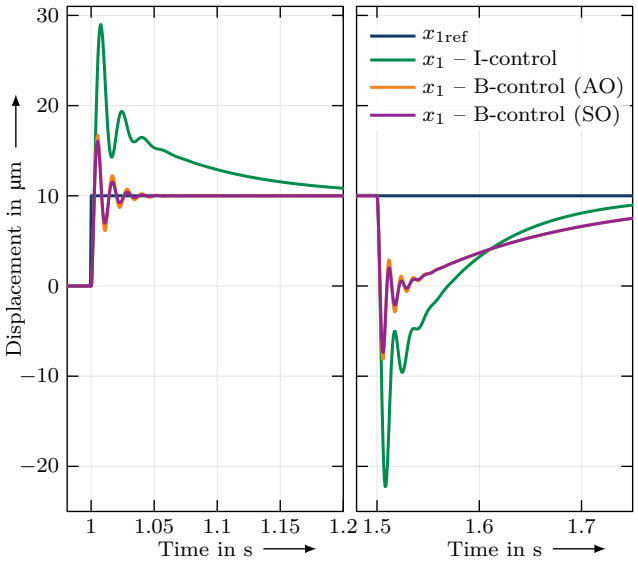

Fig. 7. Simulated command and disturbance response ($F_\mathrm{d} = 5\,\mathrm{N}$ at $t = 1.5\,\mathrm{s}$) for current control and flux density control

A. State space model

A commonly known control method is state feedback or state space control (SS-control). The system with flux density feedback from Fig. 6 can be modelled as

$$\dot{\boldsymbol{x}} = \boldsymbol{A}\boldsymbol{x} + \boldsymbol{B}u \tag{45a}$$

$$y = \boldsymbol{C}\boldsymbol{x} \tag{45b}$$

with the desired voltage values as the input $u = u^*$, position as the output $y = x$. Defining the space vector

$$\boldsymbol{x} = \begin{bmatrix} x & v & B_\mathrm{x} & u \end{bmatrix}^\mathrm{T} \tag{46}$$

where $v = \frac{\mathrm{d}x}{\mathrm{d}t}$ is the speed of the shaft and $B_\mathrm{x} = B_\mathrm{meas} - x\frac{k_\mathrm{x}}{k_\mathrm{B}}$, leads to the system's matrices

$$\boldsymbol{A} = \begin{bmatrix} 0 & 1 & 0 & 0 \\ \frac{k_\mathrm{x}}{m} & 0 & \frac{k_\mathrm{B}}{m} & 0 \\ 0 & 0 & -\frac{1}{T_\mathrm{h}} & \frac{1}{pwA_\delta} \\ 0 & 0 & 0 & -\frac{1}{T_\mathrm{VSC}} \end{bmatrix} \tag{47a}$$

$$\boldsymbol{B} = \begin{bmatrix} 0 & 0 & 0 & \frac{V_\mathrm{VSC}}{T_\mathrm{VSC}} \end{bmatrix}^\mathrm{T} \tag{47b}$$

$$\boldsymbol{C} = \begin{bmatrix} 1 & 0 & 0 & 0 \end{bmatrix} . \tag{47c}$$

Observability and controllability of the system can be proven with the Hautus lemmas

$$\operatorname{rank}\begin{pmatrix} \lambda\boldsymbol{I} - \boldsymbol{A} \\ \boldsymbol{C} \end{pmatrix} = 4 \qquad \text{and} \tag{48a}$$

$$\operatorname{rank}(\lambda\boldsymbol{I} - \boldsymbol{A}, \boldsymbol{B}) = 4 \qquad \forall\, \lambda \in \mathbb{C} \tag{48b}$$

where λ are the Eigenvalues of $\boldsymbol{A}$. The alternative state space representation with the state B_meas instead of B_x leads to controllability problems when designing the reduced observer.

Robustness is a major concern for the designed control, therefore integral state space control is designed with the structure shown in Fig. 8.

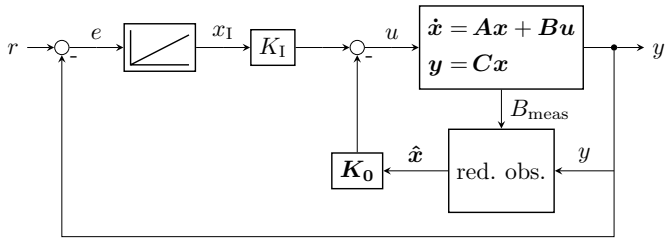

Fig. 8. Block diagram for the integral state space control with reduced observer

The additional state x_I is added at the end of the space vector. Consequently, the matrices need to be extended. Thus

$$\boldsymbol{x}_\mathrm{e} = \begin{bmatrix}\boldsymbol{x} & x_\mathrm{I}\end{bmatrix}^\mathrm{T} \tag{49a}$$

$$\boldsymbol{A}_\mathrm{e} = \begin{bmatrix}\boldsymbol{A} & \boldsymbol{0}\\ -\boldsymbol{C} & 0\end{bmatrix} \tag{49b}$$

$$\boldsymbol{B}_\mathrm{e} = \begin{bmatrix}\boldsymbol{B} & 0\end{bmatrix}^\mathrm{T} \tag{49c}$$

$$\boldsymbol{C}_\mathrm{e} = \begin{bmatrix}\boldsymbol{C} & 0\end{bmatrix} \tag{49d}$$

and

$$\dot{\boldsymbol{x}}_\mathrm{e} = \boldsymbol{A}_\mathrm{e}\boldsymbol{x}_\mathrm{e} + \boldsymbol{B}_\mathrm{e}u + \begin{bmatrix}\boldsymbol{0}\\ 1\end{bmatrix} r\,. \tag{49e}$$

With

$$u = K_\mathrm{I}x_\mathrm{I} - \boldsymbol{K}_0\boldsymbol{x} = \underbrace{\begin{bmatrix}-\boldsymbol{K}_0 & K_\mathrm{I}\end{bmatrix}}_{-\boldsymbol{K}}\boldsymbol{x}_\mathrm{e} \tag{50}$$

(49e) can be written as

$$\dot{\boldsymbol{x}}_\mathrm{e} = (\boldsymbol{A}_\mathrm{e} - \boldsymbol{B}_\mathrm{e}\boldsymbol{K})\boldsymbol{x}_\mathrm{e} + \begin{bmatrix}\boldsymbol{0}\\ 1\end{bmatrix} r\,. \tag{51}$$

Now, the poles can be placed for the extended system to get the desired behaviour.

B. Reduced observer

For state space control all states must be known, meaning that they need to be measured or observed. The state x is measured and B_x calculated as stated. The other states are found using a reduced observer. Therefore, the state vector is rearranged

$$\boldsymbol{x}_\mathrm{o} = \begin{bmatrix}\boldsymbol{x}_1\\ \boldsymbol{x}_2\end{bmatrix} \quad \text{with} \quad \boldsymbol{x}_1 = \begin{bmatrix}x\\ B_\mathrm{x}\end{bmatrix},\ \boldsymbol{x}_2 = \begin{bmatrix}v\\ u\end{bmatrix}\,. \tag{52a}$$

The resulting changes in the matrices' arrangement lead to

$$\dot{\boldsymbol{x}}_\mathrm{o} = \begin{bmatrix}\dot{\boldsymbol{x}}_1\\ \dot{\boldsymbol{x}}_2\end{bmatrix} = \begin{bmatrix}\boldsymbol{A}_{11} & \boldsymbol{A}_{12}\\ \boldsymbol{A}_{21} & \boldsymbol{A}_{22}\end{bmatrix}\begin{bmatrix}\boldsymbol{x}_1\\ \boldsymbol{x}_2\end{bmatrix} + \begin{bmatrix}\boldsymbol{B}_1\\ \boldsymbol{B}_2\end{bmatrix}u^*\,. \tag{52b}$$

B_meas is used as a second output thus $\boldsymbol{y} \in \mathbb{R}^2$ with

$$\boldsymbol{y} = \begin{bmatrix}x\\ B_\mathrm{meas}\end{bmatrix} = \boldsymbol{C}_\mathrm{o}\begin{bmatrix}x\\ B_\mathrm{x}\end{bmatrix} \quad , \quad \boldsymbol{C}_\mathrm{o} = \begin{bmatrix}1 & 0\\ \frac{k_\mathrm{x}}{k_\mathrm{B}} & 1\end{bmatrix} \tag{52c}$$

and

$$\boldsymbol{x}_1 = \boldsymbol{C}_0^{-1}\boldsymbol{y}\,. \tag{52d}$$

From (52b) follows

$$\dot{\boldsymbol{x}}_2 = \boldsymbol{A}_{21}\boldsymbol{x}_1 + \boldsymbol{A}_{22}\boldsymbol{x}_2 + \boldsymbol{B}_2u^* \tag{53a}$$

$$\bar{\boldsymbol{y}} \coloneqq \boldsymbol{A}_{12}\boldsymbol{x}_2 = \dot{\boldsymbol{x}}_1 - \boldsymbol{A}_{11}\boldsymbol{x}_1 - \boldsymbol{B}_1u^* \tag{53b}$$

with the newly virtual output $\bar{\boldsymbol{y}}$. For the estimated part $\hat{\boldsymbol{x}}_2$ of the space vector is described by

$$\dot{\hat{\boldsymbol{x}}}_2 = \boldsymbol{A}_{21}\boldsymbol{x}_1 + \boldsymbol{A}_{22}\hat{\boldsymbol{x}}_2 + \boldsymbol{B}_2u^* + \boldsymbol{L}(\bar{\boldsymbol{y}} - \hat{\bar{\boldsymbol{y}}}) \tag{54a}$$

$$\hat{\bar{\boldsymbol{y}}} \coloneqq \boldsymbol{A}_{12}\hat{\boldsymbol{x}}_2 \tag{54b}$$

with the observer gain matrix $\boldsymbol{L} \in \mathbb{R}^{2\times 2}$. Defining the observer error as $\boldsymbol{e}_2 \coloneqq \boldsymbol{x}_2 - \hat{\boldsymbol{x}}_2$, differentiating with respect to time and substituting (53) and (54) lead to the observer dynamics

$$\dot{\boldsymbol{e}}_2 = \dot{\boldsymbol{x}}_2 - \dot{\hat{\boldsymbol{x}}}_2 = (\boldsymbol{A}_{22} - \boldsymbol{L}\boldsymbol{A}_{12})\boldsymbol{e}_2\,. \tag{55}$$

The poles of $(\boldsymbol{A}_{22} - \boldsymbol{L}\boldsymbol{A}_{12})$ can be set analogously to the poles of $(\boldsymbol{A}_\mathrm{e} - \boldsymbol{B}_\mathrm{e}\boldsymbol{K})$. The observer settles faster than the system, if the poles are further left in the complex s-plane. The poles $s_{1/2}$ with a three times larger real part lead to satisfying results.

Using (53b) and (54b) in (54a) leads to

$$\begin{aligned}\dot{\hat{\boldsymbol{x}}}_2 = {}& (\boldsymbol{A}_{21} - \boldsymbol{L}\boldsymbol{A}_{11})\boldsymbol{x}_1 + (\boldsymbol{A}_{22} - \boldsymbol{L}\boldsymbol{A}_{12})\hat{\boldsymbol{x}}_2\\ & + (\boldsymbol{B}_2 - \boldsymbol{L}\boldsymbol{B}_1)u^* + \boldsymbol{L}\dot{\boldsymbol{x}}_1\end{aligned} \tag{56}$$

and with newly defined $\bar{\boldsymbol{x}}_2 \coloneqq \hat{\boldsymbol{x}}_2 - \boldsymbol{L}\boldsymbol{x}_1$ to the final observer equations

$$\begin{aligned}\dot{\bar{\boldsymbol{x}}}_2 = {}& [\boldsymbol{A}_{21} - \boldsymbol{L}\boldsymbol{A}_{11} + (\boldsymbol{A}_{22} - \boldsymbol{L}\boldsymbol{A}_{12})\boldsymbol{L}]\,\boldsymbol{x}_1\\ & + (\boldsymbol{A}_{22} - \boldsymbol{L}\boldsymbol{A}_{12})\bar{\boldsymbol{x}}_2 + (\boldsymbol{B}_2 - \boldsymbol{L}\boldsymbol{B}_1)u^*\end{aligned} \tag{57a}$$

$$\hat{\boldsymbol{x}}_2 = \bar{\boldsymbol{x}}_2 + \boldsymbol{L}\boldsymbol{x}_1\,. \tag{57b}$$

C. Pole assignment

There are different techniques to place the poles of (51) and by that define the behaviour of the closed loop system. A straight forward approach is the pole assignment or pole placement. Theoretically, the poles of $(\boldsymbol{A}_\mathrm{e} - \boldsymbol{B}_\mathrm{e}\boldsymbol{K})$ can be placed arbitrarily by choosing $\boldsymbol{K}$ appropriate. Restrictions and boundary conditions limit the poles' positions. Two popular placement variants will be discussed subsequently. For both can be said, that a negative real part of about 350 1/rad results in the maximum controller gain.

First, the poles are placed in a *funnel* on the left half of the s-plane [11]. The over shoot amplitude and time can be set by placing one dominant complex pole pair and the others further left. The left most position is limited by the maximum controller gain and the actuator dynamics, the imaginary part by the desired damping. With a damping $d = 0.4$ and the negative real part $\omega_0 d = 113$ 1/rad the dominant poles can be calculated

$$s_{1/2} = -\omega_0 d \pm \mathrm{j}\ \omega_0\sqrt{d^2 - 1}\,. \tag{58}$$

The poles $s_{3/4}$ are placed further left (with $3\omega_0$) and $s_5 = \mathrm{Re}\{s_3\}$. This configuration results in a very good command response and decent disturbance response as shown in Fig. 9.

An alternative placement strategy is the *Butterworth pattern*. It describes that n poles are paced on a semicircle in the left complex s-plane with the radius r to the origin. The poles can be found by solving

$$\left(\frac{s}{r}\right)^{2n} = (-1)^{n+1}\,. \tag{59}$$

The Butterworth pattern is known to lead to an efficient behaviour in regards to the control effort [12].

With higher n the real part of the poles decreases. This leads to reduced dynamics and instability. Therefore, the poles closest to the imaginary axis, calculated by (59), are moved further left by doubling the real part. Fig. 9 shows, that this adjusted Butterworth pattern leads to a good command response but moderate disturbance response.

D. Optimal control

For optimal control the feedback matrix $\boldsymbol{K}$ is calculated in a way, that the cost function

$$J(t) = \int_0^t \left[\boldsymbol{x}^{\mathrm{T}}(\tau)\boldsymbol{Q}\boldsymbol{x}(\tau) + \boldsymbol{u}^{\mathrm{T}}(\tau)\boldsymbol{R}\boldsymbol{u}(\tau)\right] \mathrm{d}\,\tau \tag{60}$$

with

$$\boldsymbol{u}(t) = -\boldsymbol{K}\boldsymbol{x}(t) \tag{61}$$

is minimized [13]. The optimal control is a compromise between minimizing the states (left addend) and the control signal (right addend). The positive definite matrices $\boldsymbol{Q}$ and $\boldsymbol{R}$ weight the two summands.

Differentiating (60) and some substitutions (see [13] for details) lead to the optimal controller gain matrix

$$\boldsymbol{K} = \boldsymbol{R}^{-1}\boldsymbol{B}^{\mathrm{T}}\boldsymbol{P} \tag{62}$$

where $\boldsymbol{P}$ is the solution of the algebraic Riccati equation

$$\boldsymbol{A}^{\mathrm{T}}\boldsymbol{P} + \boldsymbol{P}\boldsymbol{A} - \boldsymbol{P}\boldsymbol{B}\boldsymbol{R}^{-1}\boldsymbol{B}^{\mathrm{T}}\boldsymbol{P} + \boldsymbol{Q} = \boldsymbol{0}\,. \tag{63}$$

The simulation results for the optimal control with the weighting matrices

$$\boldsymbol{Q} = \begin{bmatrix} 10^5 & 0 & 0 & 0 & 0 \\ 0 & 1 & 0 & 0 & 0 \\ 0 & 0 & 100 & 0 & 0 \\ 0 & 0 & 0 & 10 & 0 \\ 0 & 0 & 0 & 0 & 10^{13} \end{bmatrix} \tag{64a}$$

$$\boldsymbol{R} = \begin{bmatrix} 10 \end{bmatrix} \tag{64b}$$

are shown in Fig. 9. The coefficients represent the "importance" of the corresponding state when solving the cost function. As can be seen from (64), the highest importance is given to the control error, followed by the position. When choosing the factors, the different units of the states need to be taken into account. The calculations are implemented with the position in meters, so that this very small values need to be compensated by high weighting factors. $\boldsymbol{R}$ considers the actuator, so higher values lead to smaller control signals.

The settling time for the command and the disturbance response is greater, but the actuator effort is reduced as Fig. 10 shows.

V. Comparison and Conclusion

The simulation results for the introduced B-control with symmetrical optimum, state space control with poles placed in an funnel and optimal control are plotted in Fig. 11. The state space control improves the overshoot of the command response and the settling time after a disturbance step significantly but with the observer and the state feedback for all five axis the computation demand rises.

Comparing the controller output in Fig. 12 shows, that the oscillation of the voltage can be reduced, especially by using optimal control. This reduces the effective frequency of the current and therefore leads to lower eddy currents. Especially the performance of thrust bearings is influenced by eddy currents [7], so that OC can be used for z-axis if stiffness is not the highest concern.

Finally, some implementation hints should be mentioned: The values of the gain matrices for the state space control differ in orders of magnitude. When using 16 bit float numbers, the discretization of the vectors causes problems which can be solved by using double precision values. The controller performance is not significantly increased when reducing the sampling time for the control loop, but with half the sampling time the system becomes unstable.

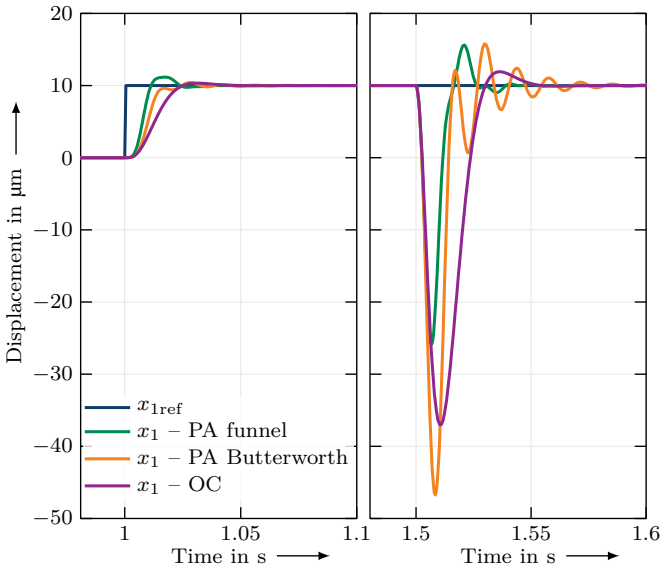

Fig. 9. Simulated command and disturbance response ($F_{\mathrm{d}} = 5\,\mathrm{N}$ at $t = 1.5\,\mathrm{s}$) for state space control with pole assignment (PA) and and optimal control (OC).

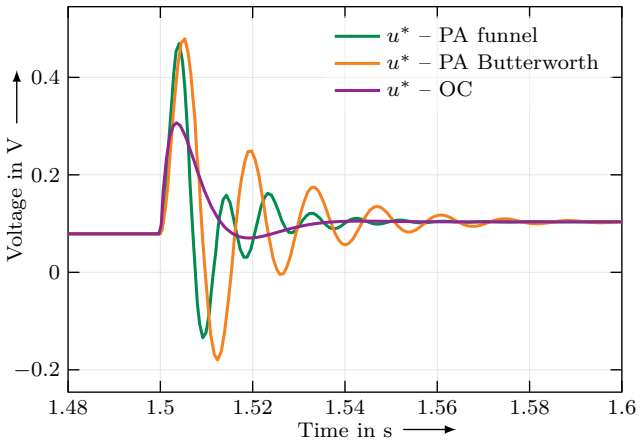

Fig. 10. Controller output (desired voltage) for x1 axis to settle a disturbance step ($F_{\mathrm{d}} = 5\,\mathrm{N}$ at $t = 1.5\,\mathrm{s}$) for state space control with pole assignment (PA) and and optimal control (OC).

VI. Acknowledgement

This work was funded by the German Research Foundation (DFG) under the grant HO 1483/62-2 and supported with funding form the excellence initiative by the German federal and state governments.

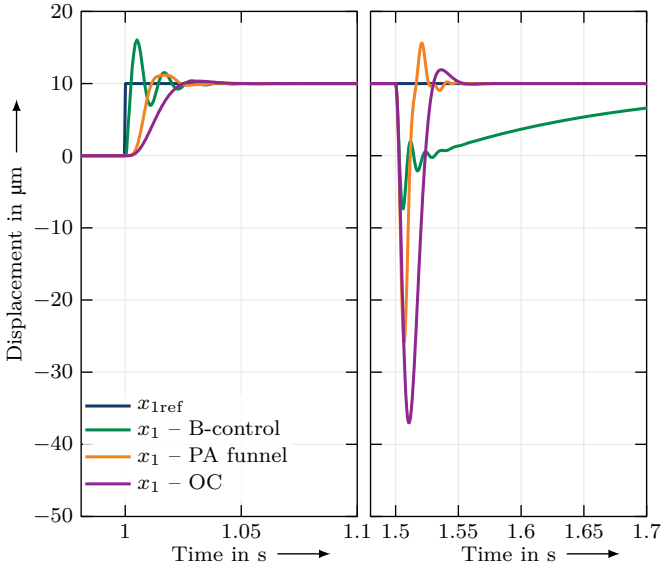

Fig. 11. Simulated command and disturbance response ($F_\mathrm{d} = 5\,\mathrm{N}$ at $t = 1.5\,\mathrm{s}$) for cascaded B-control and state space control with funnel placement and optimal control (OC)

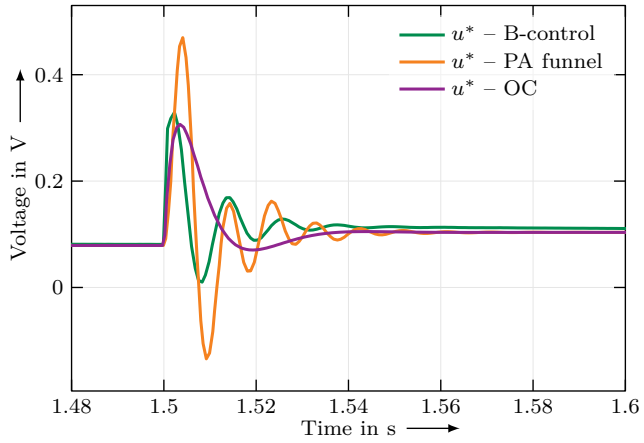

Fig. 12. Controller output (desired voltage) for x1 axis to settle a disturbance step ($F_\mathrm{d} = 5\,\mathrm{N}$ at $t = 1.5\,\mathrm{s}$) for cascaded B-control and state space control with funnel placement and optimal control (OC)

VII. References

[1] A. M. Mohamed and F. P. Emad, "A comparison between current and flux control in magnetic bearing systems," *1993 American Control Conference*, Jun. 1993, pp. 2356–2362.

[2] P. O. Jaatinen, R. P. Jastrzebski, T. Lindh, *et al.*, "Implementation of a flux-based controller for active magnetic bearing system," *2013 11th IEEE International Conference on Industrial Informatics (INDIN)*, Jul. 2013, pp. 141–145.

[3] H. Bleuler, D. Vischer, G. Schweitzer, *et al.*, "New concepts for cost-effective magnetic bearing control," *automatica*, vol. 30, no. 5, pp. 871–876, 1994.

[4] F. Bahr, M. Melzer, D. Karnaushenko, *et al.*, "Flux based control of AMBs using integrated ultra-thin flexible bismuth Hall sensors," *Proceedings of the 13th International Symposium on Magnetic Bearings (ISMB 13)*, Arlington, USA, 2012.

[5] I. J. Mönch, F. Bahr, M. Melzer, *et al.*, "Flexible Hall sensorics for flux-based control of magnetic levitation," 11, vol. 51, Nov. 2015, pp. 1–4.

[6] F. Bahr, I. Mönch, D. Ernst, *et al.*, "Direct field control of AMBs using flux feedback based on integrable Hall sensors," *Proceedings of the 15th International Symposium on Magnetic Bearings*, 2016.

[7] R. Seifert and W. Hofmann, "Completion of analytical model of active magnetic thrust bearings including asymmetric air gap field between mixed materials," *Mechanical Engineering Journal, Bulletin of the JSME*, vol. 4, no. 5, J. S. of Mechanical Engineers, Ed., pp. 1–11, 2017.

[8] G. Schweitzer, H. Bleuler, E. Maslen, *et al.*, *Magnetic Bearings: Theory, Design, and Application to Rotating Machinery*. Berlin, Heidelberg: Springer, 2009.

[9] K. J. Åström and T. Hägglund, *PID controllers: theory, design, and tuning*. Isa Research Triangle Park, NC, 1995, vol. 2.

[10] H. Lutz and W. Wendt, *Taschenbuch der Regelungstechnik*, 10th ed. Harri Deutsch, 2014.

[11] J. Lunze, *Regelungstechnik 1*, 11th ed. Springer Berlin Heidelberg, 2016.

[12] A. Tewari, *Modern Control Design: With MATLAB and Simulink*. JOHN WILEY & SONS INC, Apr. 11, 2002, 503 pp.

[13] J. Lunze, *Regelungstechnik 2*, 9th ed. Springer Berlin Heidelberg, 2016.

VIII. Biographies

Robin Liebfried received the Dipl.-Ing. degree in Electrical Engineering from TU Dresden, Germany in 2017. Since 2017, he is a postgraduate researcher and doctoral candidate at the Chair of Electrical Machines and Drives at Technische Universität Dresden. He did an exchange and research Semester at POSTECH University of Science and Technology in South Korea at the department of Electrical Machines and Drives. His research focuses on magnetic bearings, control systems and power electronics.

Wilfried Hofmann received the Dipl.-Ing. and Dr.-Ing degrees in Electrical Engineering from TU Dresden, Germany, in 1978 and 1984, respectively. He was a Development Engineer with Elpro AG (1982-89). He was the Chair of the Department of Electrical Machines and Drives, TU Chemnitz, Germany (1992-2007). Since 2007, he has been the Head of the Department of Electrical Machines and Drives, TU Dresden. He has published over 260 papers and 60 patents and is the author or co-author of four technical books. His main research areas are electromagnetic energy conversion, mechatronics and motion control, control of ac machines, power electronics, and renewable energy conversion systems. Dr. Hofmann is member of the German Academy of Science and Engineering (acatech) and of the Saxonia Academy of Science, Senior member of IEEE, VDE, VDI, Steering Committee of European Power Electronics and Drives Association (EPE).